

# RSC Advances



This is an *Accepted Manuscript*, which has been through the Royal Society of Chemistry peer review process and has been accepted for publication.

*Accepted Manuscripts* are published online shortly after acceptance, before technical editing, formatting and proof reading. Using this free service, authors can make their results available to the community, in citable form, before we publish the edited article. This *Accepted Manuscript* will be replaced by the edited, formatted and paginated article as soon as this is available.

You can find more information about *Accepted Manuscripts* in the [Information for Authors](#).

Please note that technical editing may introduce minor changes to the text and/or graphics, which may alter content. The journal's standard [Terms & Conditions](#) and the [Ethical guidelines](#) still apply. In no event shall the Royal Society of Chemistry be held responsible for any errors or omissions in this *Accepted Manuscript* or any consequences arising from the use of any information it contains.



## Nanostructured $\text{Co}_x\text{Ni}_{1-x}$ bimetallic alloys for high efficient and ultrafast adsorption: experiments and first-principles calculations†

Received 00th January 20xx,  
Accepted 00th January 20xx

DOI: 10.1039/x0xx00000x

www.rsc.org/

Haiming Sun, Xijia Yang, Lijun Zhao\*, Yue Li, Jiamu Zhang, Lu Tang, Yining Zou, Cong Dong, Jianshe Lian\* and Qing Jiang

Use change of composition and surface defects of  $\text{Co}_x\text{Ni}_{1-x}$  bimetallic alloy prepared at room temperature to improve their adsorption capabilities. Congo red (CR) was used to evaluate the  $\text{Co}_x\text{Ni}_{1-x}$  bimetallic alloys' adsorption capabilities. At 100  $\text{mg L}^{-1}$  of initial CR concentration, 1000  $\text{mg g}^{-1}$  of adsorption capacity could be achieved by the  $\text{Co}_x\text{Ni}_{1-x}$  nanoparticles in time range of 2 to 20 minutes. Here,  $\text{Co}_{0.6}\text{Ni}_{0.4}$  bimetallic alloy shows the best adsorption efficiency, reaching 1000  $\text{mg g}^{-1}$  at 2 min. Furthermore, density functional theory (DFT) simulations were introduced to understand why  $\text{Co}_{0.6}\text{Ni}_{0.4}$  bimetallic alloy had better adsorption efficiency than monometal Co and Ni. Based on DFT simulations, large surface energy, low work function and high reducibility of  $\text{Co}_{0.6}\text{Ni}_{0.4}$  bimetallic alloy may be responsible for its high adsorption capability and efficiency. By a further investigation on surface electronic structure, it can be found that the chemical composition and surface defects have influences on  $d$ -band center, and a proper  $d$ -band center may facilitate to both the high rate of electrons transfer to adsorbate and removal of surface intermediate. The combination of experiment and DFT simulations proved that the adsorption ability of  $\text{Co}_{0.6}\text{Ni}_{0.4}$  bimetallic alloy is better than that of single metal, and shows promise as commercial scale magnetic adsorbent.

### 1. Introduction

Magnetic Co, Ni and their composites have been extensively applied in many technological fields, such as lithium-ion batteries, catalysis, adsorption and so on,<sup>1-6</sup> owing to their lower cost, good stability, easy magnetic separation and unique chemical performance. Among others, bimetallic nanostructured materials can be considered as a new type of material, some of their properties can be greatly enhanced by the synergistic effects of mixture, which arose from the presence of two metals and intimate contact between them.<sup>7-9</sup> The rich diversity of composition and structure may meet the desire to fabricate materials with well-defined, controllable properties. Therefore, bimetallic nanoparticles have attracted a tremendous attention from worldwide researchers in recent years.<sup>10-12</sup> Due to the complicated and multiform structures of bimetallic materials, one can distinguish them by a statistical chemical distribution of the two metals in the material. According to this method, three main types of structures can be identified for bimetallic materials, that is, core/shell, heterostructure, or intermetallic and alloyed structures.<sup>13</sup>

With increasing demand for environmentally friendly and

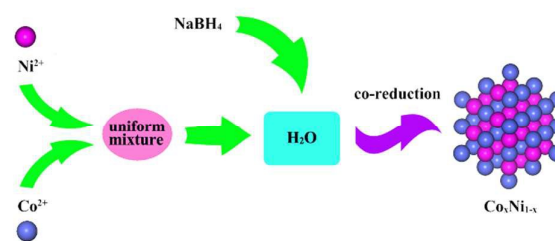
sustainable development, intensive studies have been devoted to sewage treatment by the promising methods such as chemical catalytic oxidation, acidification, coagulation, adsorption, etc.<sup>2, 14-17</sup> Among the above-mentioned methods, adsorption could be the most widely used due to low initial cost, high flexibility, simple design and operation, easy automation, lack of sensitivity to toxic pollutants and the possibility to operate at very low concentrations.<sup>18</sup> Congo Red (CR), a classical anionic diazo dye, is difficult to be biodegraded owing to its structural stability. Recently, the removal of CR from aqueous solution by the use of transition metal oxides adsorbent (such as  $\text{Cu}_2\text{O}$  and  $\text{ZrO}_2$ ) have been reported.<sup>19,20</sup> Although they showed excellent adsorption property, but the long operation period and complicated separation method limited their application in practice. Co nanoparticles, as a typical ferromagnetic material, while used as adsorbent they could be easily separated from liquid phase by a magnet after adsorption process. In a previous study, we reported air-stable cobalt metal nanoparticles exhibit high efficient adsorption for Congo red (CR).<sup>21</sup> Inspired by the advantages of bimetallic, we expect to introduce a secondary metal into the air-stable Co system to improve the adsorption performance. As it's known to all, Ni has similar atom radius and chemical properties with Co, and it has been reported that the intersolubility of Co and Ni is extremely high. Herein, bimetallic magnetic  $\text{Co}_x\text{Ni}_{1-x}$  nanoparticles were successfully synthesized by a room temperature  $\text{NaBH}_4$  reduction method, more excellent adsorption performance for CR would achieve by adjusting the composition of bimetallic particles.

Key Laboratory of Automobile Materials (Jilin University), Ministry of Education and School of Materials Science and Engineering, Jilin University, Changchun 130022, China. E-mail: [lijunzhao@jlu.edu.cn](mailto:lijunzhao@jlu.edu.cn); [liansj@jlu.edu.cn](mailto:liansj@jlu.edu.cn)

†Electronic Supplementary Information (ESI) available: Characterization and adsorption experiment details. See DOI:10.1039/x0xx00000x

Despite extensive experimental researches provide considerable insight into structure and mechanism of adsorption thus helping to bridge the connection between the molecules and macroscopic world, principles of higher order organization of molecules are desired for further investigation. Experimental studies mainly concerned the adsorption capacities and adsorption kinetics, while seldom investigations were devoted to research the relationship between high-performance adsorption and surface properties of adsorbent. Nowadays, considerable effort has been increasingly directed toward closing the gap between theory and practice, for example, first-principles studies based on density functional theory (DFT) have played an important role in predicting and investigating the property of advanced material. Recently, DFT calculations are used to predict and illustrate the relations between surface property and surface reaction. When *h*-BN monolayer was deposited on the Ni (111) support, it can be used as a novel catalyst for CO oxidation.<sup>22</sup> Furthermore, the electronic structure and dynamical nature of H<sub>2</sub>O/Pt (111) and H<sub>2</sub>O/Ni (111) interfaces were studied to demonstrate the effects of aqueous phase on the hydrogenation of phenol.<sup>23</sup> With the aid of the DFT simulations, the role of aluminum in reducing sulfur poisoning on Ni<sub>3</sub>Al compared to pure Ni materials are also investigated.<sup>24</sup> N-nitrosodimethylamine (NDMA) reaction with coadsorbed hydrogen on the Ni (111) surface has been investigated in the low coverage regime.<sup>25</sup> It's widely known that crystal facet is an important feature of crystalline materials, different crystal facets may have divergent electronic structures performing different surface physical and chemical property. Surface energy and work function are two most fundamental properties of a metallic surface, and their determination is of great importance in the understanding of a wide range of surface phenomena, including growth rate, catalytic behavior, adsorption and so on.<sup>26</sup> On the other hand, numerous experimental and theoretical studies have been carried out to study the kinetics of transition metal involved oxygen reduction reaction (ORR),<sup>27-29</sup> where the *d*-band energy of metal surface is the key parameter which determines the kinetics of ORR. In the current situation, as the accuracy of calculations has improved considerably, we may use first-principles calculations as a guide. Herein, the obtained theoretical results, such as the surface energy, work function and electronic structure, will present a detailed atomic level understanding of the mechanism and process of adsorption.

In the present study, we put forward a room-temperature NaBH<sub>4</sub> reduction method for fabricating air-stable Co<sub>x</sub>Ni<sub>1-x</sub> bimetallic alloy nanoparticles. The preparation procedure is shown in Scheme 1. By adjusting the composition of bimetallic nanoparticles, the adsorption capability for pollutants (here Congo red, CR) is studied. Herein, Co<sub>x</sub>Ni<sub>1-x</sub> alloy nanoparticles with ferromagnetic behavior could remove CR very quickly and efficiently, and then they could be separated from wastewater by a magnet. Since the adsorption property is mostly related to the surface properties, first principles calculations based on DFT is applied to study the electronic structure and related surface properties of theoretical surface models, presenting a



**Scheme 1** Schematic illustration of the preparation process of the Co<sub>x</sub>Ni<sub>1-x</sub> bimetallic alloy nanoparticles.

possible explanation of the adsorption process, capability and mechanism from an atomic level understanding.

## 2. Experimental and Computational Details

### 2.1 Chemicals and Synthesis

All chemicals were of analytical grade and used as received. The chemicals were purchased from Beijing Chemicals Co. (Beijing, China). CoCl<sub>2</sub>·6H<sub>2</sub>O and NiCl<sub>2</sub>·6H<sub>2</sub>O were used as cobalt and nickel sources, respectively. And NaBH<sub>4</sub> is reducing agent. For the adsorption experiment, the adsorbate CR (a typical organic contaminant) was purchased from Tianjin Kermel Chemical Co. (Tianjin, China).

In a typical procedure ascribed in scheme 1, a calculated amount of CoCl<sub>2</sub>·6H<sub>2</sub>O and NiCl<sub>2</sub>·6H<sub>2</sub>O were first mixed to form a uniform mixture. Then, the mixture and a certain amount of NaBH<sub>4</sub> were added into a beaker of 20 mL of deionized water at the same time. Experimentally, we had found that the molar ratio of M<sup>2+</sup> (Co<sup>2+</sup> and Ni<sup>2+</sup>)/NaBH<sub>4</sub> were chosen to be 0.32:1 for the formation of nanostructured Co<sub>x</sub>Ni<sub>1-x</sub> bimetallic alloy. After the addition, a black product was formed immediately in the bottom of the beaker with the hydrogen release. The reaction ends with no more bubbles arose, and then we collected the black powders with a magnet and washed them with deionized water and ethanol several times. Finally, the powders were dried at room temperature in air for 24 h. Co<sub>x</sub>Ni<sub>1-x</sub> nanoparticles with different *x* (*x* = 0, 0.2, 0.4, 0.6, 0.8 and 1) were prepared with the same procedure.

### 2.2 Calculation Method

All calculations are performed on the Cambridge serial total energy package (CASTEP) code,<sup>30-32</sup> which is based on density functional theory (DFT) using ultrasoft-pseudopotential method. The exchange and correlation interactions are described by the Perdew-Wang 1991 (PW91)<sup>33</sup> function within the generalized-gradient approximation (GGA).<sup>34</sup> The valence electronic configurations for Co and Ni are 3d<sup>7</sup>4s<sup>2</sup> and 3d<sup>8</sup>4s<sup>2</sup>, respectively. The three unit cells of bulk *fcc*-Co, *fcc*-Ni and *fcc*-Co<sub>0.5</sub>Ni<sub>0.5</sub> (the bulk *fcc*-Co<sub>0.5</sub>Ni<sub>0.5</sub> structure is modeled by replacing a half of the Ni atoms in face-centered-cubic lattice by Co atoms) are ultra-finely relaxed. The models used in the calculation are shown in Fig. 1. A *k*-point mesh of 8×8×8 and cutoff energy of 380 eV are used in the calculations. The calculated lattice pa-

parameters of bulk *fcc*-Co and *fcc*-Ni are 3.547 Å and 3.537 Å, respectively, which are in fair agree with previous theoretical results.<sup>35</sup> The current calculations present the lattice constants of  $a=c=3.507$  Å and  $b=3.614$  Å for bulk *fcc*-Co<sub>0.5</sub>Ni<sub>0.5</sub>, which demonstrates that the mutual doping of Co and Ni induces a contraction in  $a$  and  $c$ , and an expansion in  $b$  compared with bulk *fcc*-Co and *fcc*-Ni.

The surfaces are obtained by cutting the relaxed bulk models along [111], [110] and [100] directions, forming (111), (110) and (100) surfaces, respectively. All the surface models are built with a slab thickness of seven atomic layers, the bottom four layers are fixed at their position in the bulk, while the upper three layers are allowed to relax freely. A vacuum thickness of 20 Å is used to negate the interactions between periodic slabs. For Co<sub>0.5</sub>Ni<sub>0.5</sub> (111) surface, we also calculate three vacancy defect models named  $V_{Co}$ ,  $V_{Ni}$  and  $V_{CoNi}$ , representing removing a Co atom, a Ni atom and both of them in the first layer, respectively. The supercell models with (2×2) surface are used in the calculation. The surface models are also presented in Fig. 1. Spin polarization is considered in all calculations. The cutoff energy of 400 eV and k-point meshes of 10×10×1 are used in the surface models calculations. The convergence in energy, maximum force, maximum stress and maximum displacement tolerances are set as  $2.0 \times 10^{-5}$  eV/atom, 0.05 eV/Å, 0.1 GPa and 0.002Å, respectively.

### 3. Results and discussion

#### 3.1 Characterization of Co<sub>x</sub>Ni<sub>1-x</sub> alloy nanoparticles

Fig. 2a shows the XRD patterns of the synthesized Co<sub>x</sub>Ni<sub>1-x</sub> alloy nanoparticles with different  $x$  ( $x=0.0, 0.2, 0.4, 0.6, 0.8$  and  $1.0$ ), the diffraction peaks of *fcc*-Ni (JPCDS no.04-0850), *fcc*-Co (JPCDS no.15-0806) and *hcp*-Co (JPCDS no.05-0727) are marked on the bottom. For all the samples, the major diffraction peaks are located at about  $2\theta=44^\circ$ , which can be index to the *fcc*-Ni or *fcc*-Co (111) plane.

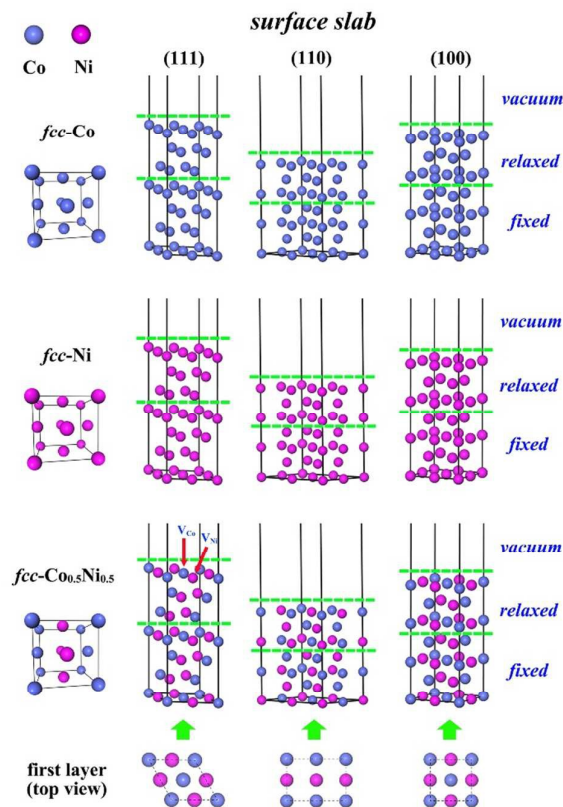


**Fig. 1** First row: models of bulk *fcc*-Co, Co (111), Co (110) and Co (100), respectively. Second row: models of bulk *fcc*-Ni, Ni (111), Ni (110) and Ni (100), respectively. Third row: models of bulk *fcc*-Co<sub>0.5</sub>Ni<sub>0.5</sub>, Co<sub>0.5</sub>Ni<sub>0.5</sub> (111), Co<sub>0.5</sub>Ni<sub>0.5</sub> (110) and Co<sub>0.5</sub>Ni<sub>0.5</sub> (100), respectively. (The atoms marked  $V_{Co}$  and  $V_{Ni}$  represent the vacancy defect positions.) Last row: top view of first layer corresponding to the three surface slabs of *fcc*-Co<sub>0.5</sub>Ni<sub>0.5</sub> system.

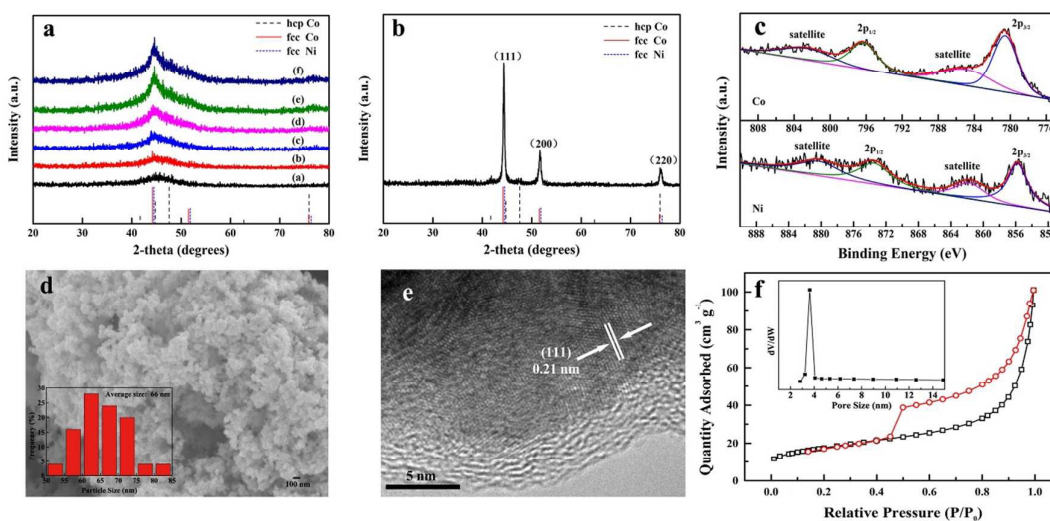


**Fig. 2** a) XRD patterns of Co<sub>x</sub>Ni<sub>1-x</sub> nanoparticles: (a) Co, (b) Co<sub>0.8</sub>Ni<sub>0.2</sub>, (c) Co<sub>0.6</sub>Ni<sub>0.4</sub>, (d) Co<sub>0.4</sub>Ni<sub>0.6</sub>, (e) Co<sub>0.2</sub>Ni<sub>0.8</sub> and (f) Ni. b) XRD patterns of Co<sub>0.6</sub>Ni<sub>0.4</sub> nanoparticles after treated at 773 K for 2 h in argon atmosphere. c) XPS survey spectra for Co 2p and Ni 2p of Co<sub>0.6</sub>Ni<sub>0.4</sub> nanoparticles. d) SEM image and particles sizes distribution (inset) of Co<sub>0.6</sub>Ni<sub>0.4</sub> nanoparticles. e) HRTEM image of Co<sub>0.6</sub>Ni<sub>0.4</sub> nanoparticles. f) The nitrogen adsorption-desorption isotherm and pore-size distribution (inset) of Co<sub>0.6</sub>Ni<sub>0.4</sub> nanoparticles.

Other diffraction peak can't be clearly observed and the peaks are broad and diffuse. These characteristics indicate that the obtained sample of Ni,  $\text{Co}_x\text{Ni}_{1-x}$  and Co are poor crystallization and in fact are the mixture of *fcc*- $\text{Co}_x\text{Ni}_{1-x}$  nano-sized crystal and amorphous  $\text{Co}_x\text{Ni}_{1-x}$ . This mixture of crystal and amorphous is often observed from the structure of electroless Ni-P alloy with intermediate P content.<sup>36</sup> As it's known to all, in normal conditions, cobalt exists mainly in *hcp* structure, but the observation of *fcc*-Co nanoparticles also has been reported.<sup>37</sup> In our experiment condition, pure Co exists mainly in *fcc* structure. To further verify the structure of the nanoparticles, the as-prepared  $\text{Co}_{0.6}\text{Ni}_{0.4}$  nanoparticles are annealed at 773 K for 2 h in argon atmosphere, and the resulted XRD is shown in Fig. 2b. After annealing, the sample is well crystallized and other peaks emerge. Even in this case, the  $\text{Co}_{0.6}\text{Ni}_{0.4}$  nanoparticles still exist in *fcc* structure (carefully observed, it likes *fcc*-Ni more than *fcc*-Co), where the Co and Ni atoms are distributed homogeneously or randomly at the Ni position.<sup>38,39</sup> X-ray photoelectron spectroscopy (XPS) spectra (Fig. 2c) of the  $\text{Co}_{0.6}\text{Ni}_{0.4}$  nanoparticles exhibit the coexistence of Co and Ni. The Co  $2p_{3/2}$  and  $2p_{1/2}$  features with binding energies of 780.6 eV and 796.2 eV, respectively, can be attributed to CoO.<sup>40</sup> And the Ni  $2p_{3/2}$  and  $2p_{1/2}$  features with binding energies of 855.8 eV and 873.1 eV, respectively, can be attributed to NiO.<sup>41</sup> It's worthy of noting that XPS data reflect only the surface information of the as-synthesized  $\text{Co}_{0.6}\text{Ni}_{0.4}$  nanoparticles, due to the limited penetration depth of XPS (0.5~3 nm). According to the XRD data of  $\text{Co}_{0.6}\text{Ni}_{0.4}$  before and after treated at 773 K for 2 h in argon atmosphere, there are no peaks associated with the reflections of metal oxides. It is rational to assume that only a very small amount of metal oxides is present on the surfaces of the nanoparticles, which are formed by air passivation (XPS results) as mentioned in the previous report of Ni-Fe nanocatalysts synthesized with similar approach.<sup>5</sup> It was demonstrated that for Ni-Co alloy, only when Co content is higher than 66%, a small

amount of *hcp*-Co can be observed.<sup>42</sup> In the present case, comparing with the main peak positions of *fcc*-Co (Ni) and *hcp*-Co, it is believed that the sample of  $\text{Co}_{0.8}\text{Ni}_{0.2}$  and Co (curve (b) and (a) in Fig. 2a) should be the mixture of *fcc*-Co (Ni) and *hcp*-Co and amorphous.

The morphology of the  $\text{Co}_x\text{Ni}_{1-x}$  alloy nanoparticles is examined by SEM as shown in Fig. 2d and Fig. S1. Obviously, all the samples are composed of agglomerate nanoparticles. In the present process, without any foreign dispersant, just using the inorganic Co (II) and Ni (II) salts as the metal reactant, the aggregation of nanoparticles is inescapability. Fig. 2d (inset) and Fig. S1 present the size distributions and average particle sizes of the samples, which are estimated from SEM micrograph and calculated by the software Nano Measurer 1.2. As the decrease of Co content, the dispersibility of particles improved. Moreover, it is noted that the Co nanoparticles have the largest particle size while the Ni nanoparticles are with the smallest. As the Co content decreases from 1 to 0, the particle size reduces gradually, which may be attributed to the weaker magnetism of Ni than Co. Hence, the decrease of Co content in samples leads to better dispersion and relatively regular particulate arrangement.<sup>39</sup> The reduction of particle size may explain as the introduction of Ni into the crystal causes the mismatch of the lattice, which will restrain the growth of crystal. Further insight into the structure of the  $\text{Co}_{0.6}\text{Ni}_{0.4}$  nanoparticles was obtained with HRTEM. Fig. 2e clearly showed that the particles were poor crystallized with amorphous surface. The interlayer spacing of the lattice fringes of the presented  $\text{Co}_{0.6}\text{Ni}_{0.4}$  particle is 0.21 nm, which is consistent with the *fcc*-Ni (or Co) (111) plane. This is agree with the analysis of XRD, in the nanoparticles, nano-sized crystal and amorphous are coexistence. And we consider the amorphous surface originating from the abundant vacancy defects formed during the room tempera-

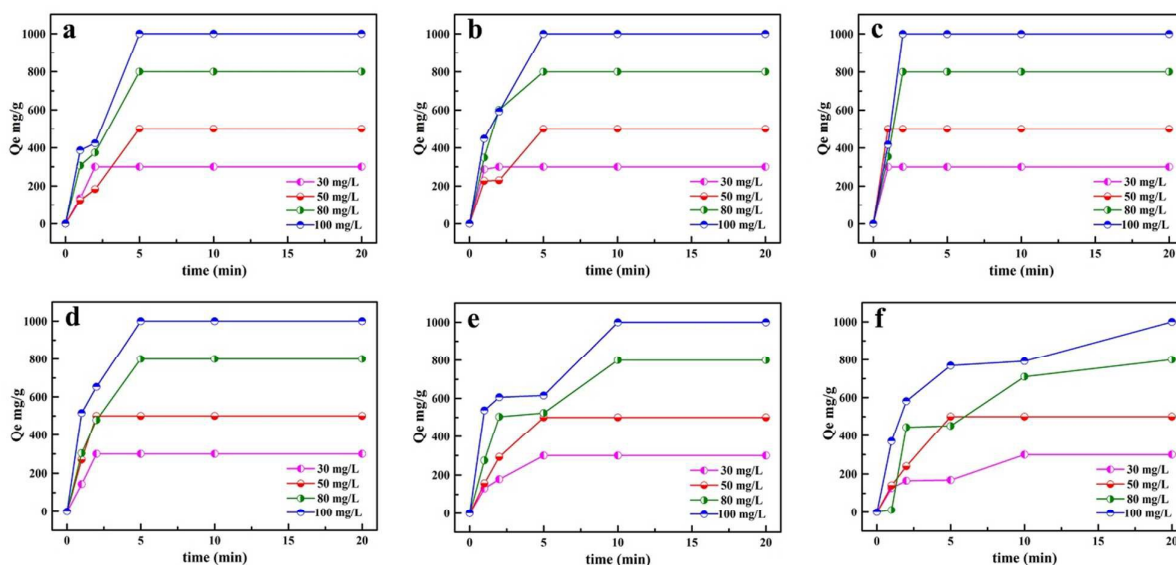


Fig. 3 Effect of initial dye concentration on CR removal: a) Co, b)  $\text{Co}_{0.8}\text{Ni}_{0.2}$ , c)  $\text{Co}_{0.6}\text{Ni}_{0.4}$ , d)  $\text{Co}_{0.4}\text{Ni}_{0.6}$ , e)  $\text{Co}_{0.2}\text{Ni}_{0.8}$  and f) Ni.

ture synthesis process. To investigate the specific surface area and pore size of the as-prepared  $\text{Co}_{0.6}\text{Ni}_{0.4}$  nanoparticles,  $\text{N}_2$  adsorption-desorption experiments were carried out. The relatively high BET surface areas of  $60.6 \text{ m}^2 \text{ g}^{-1}$  is determined from Fig. 2f, the adsorption and desorption isotherms could be categorized as type IV with a hysteric loop. The pore size distribution calculated by the BJH model was centered at 3.6 nm (Fig. 2f, inset). These pores are actually attributed to the agglomeration of the nanoparticles, and this is consistent with that observed in SEM image (Fig. 2d).

### 3.2 CR removal from aqueous solution

**Adsorption ability.** To investigate the adsorption property of the as-synthesized  $\text{Co}_x\text{Ni}_{1-x}$  nanoparticles, a series adsorption experiments for CR (a typical organic pollutant) are carried out. Fig. 3 gives the adsorption ability of the as-synthesized  $\text{Co}_x\text{Ni}_{1-x}$  nanoparticles with different initial CR concentrations (30, 50, 80 and  $100 \text{ mg L}^{-1}$ ) in the time range from 0 to 20 min. Experimental results indicate that all the samples can completely remove CR from the solution, even the initial CR concentration is increased to  $100 \text{ mg L}^{-1}$ . The final adsorption capability is increased from 300 to  $1000 \text{ mg g}^{-1}$  when the initial CR concentration ranges from 30 to  $100 \text{ mg L}^{-1}$ . Ni nanoparticles have the lowest absorption efficiency (20 min) and Co nanoparticles have much higher absorption efficiency (5min). But, the absorption efficiency does not monotonously decrease with the decreasing of Co content. The samples  $\text{Co}_{0.8}\text{Ni}_{0.2}$  and  $\text{Co}_{0.4}\text{Ni}_{0.6}$  have the same absorption efficiency as Co, while the sample  $\text{Co}_{0.6}\text{Ni}_{0.4}$  has the highest absorption efficiency, it absorbs all the CR of  $100 \text{ mg L}^{-1}$  in only 2 min, 2.5 times higher than those

of Co and its two neighbors ( $\text{Co}_{0.8}\text{Ni}_{0.2}$  and  $\text{Co}_{0.4}\text{Ni}_{0.6}$ ). For a further investigation, the adsorption property of  $\text{Co}_{0.6}\text{Ni}_{0.4}$  nanoparticles after annealing was also tested with the initial CR concentration of  $100 \text{ mg L}^{-1}$ , and the results are shown in Fig. 4a. Obviously, the annealed  $\text{Co}_{0.6}\text{Ni}_{0.4}$  nanoparticles reach adsorption equilibrium of  $687 \text{ mg g}^{-1}$  at 20 min. Compared with the sample before annealing, the decreased adsorption capacity may be caused by the well-crystallized nanoparticles and the growth of grains.

**Magnetic properties.** The magnetic properties of the as-synthesized  $\text{Co}_x\text{Ni}_{1-x}$  nanoparticles are characterized by VSM at ambient temperature. The corresponding hysteresis loops are given in Fig. 4b, which shows that all the samples exhibit typical ferromagnetic behavior, and the values of saturation magnetization ( $M_s$ ), residual magnetization ( $M_r$ ), and coercivity ( $H_c$ ) are listed in Table S1. The values of  $M_s$ ,  $M_r$  and  $H_c$  for the Co nanoparticles are  $78.3 \text{ emu g}^{-1}$ ,  $20 \text{ emu g}^{-1}$  and  $200 \text{ Oe}$ , respectively. A decrease of Co content leads to monotonic decrease in  $M_s$ ,  $M_r$  and  $H_c$ . As for the pure Ni nanoparticles, the values of  $M_s$ ,  $M_r$  and  $H_c$  reduce to  $3.9 \text{ emu g}^{-1}$ ,  $1.2 \text{ emu g}^{-1}$  and  $137 \text{ Oe}$ , respectively. Compared with the bulk counterparts of Co and Ni, the  $\text{Co}_x\text{Ni}_{1-x}$  nanoparticles synthesized by a quick reduction process at room temperature show relatively lower  $M_s$  and higher  $H_c$  values. The decreased  $M_s$  and increased  $H_c$  of  $\text{Co}_x\text{Ni}_{1-x}$  nanoparticles may be attributed to the particles prepared at room temperature with incomplete crystallization and small size. The magnetic properties endow  $\text{Co}_x\text{Ni}_{1-x}$  nanoparticles with the ability of magnetic separation, which plays a key role in practical applications. Herein, the  $\text{Co}_x\text{Ni}_{1-x}$  powders can be suspended in CR aqueous solution and conveniently separated by using a magnet after adsorption reaction.

**Adsorption kinetics.** The adsorption kinetic models were applied to interpret the experimental data to determine the controlling mechanism of CR adsorption. Herein, Pseudo-second-order was used to test dynamical experimental data.

The Pseudo-second-order kinetic model of Ho and McKay<sup>43</sup> is written as:

$$\frac{t}{q_t} = \frac{1}{K_2 q_e^2} + \frac{t}{q_e} \quad (1)$$

where  $q_t$  is the amount of dye adsorbed per unit of adsorbent ( $\text{mg g}^{-1}$ ) at time  $t$ ,  $q_e$  is the equilibrium adsorption capacity per unit of adsorbent ( $\text{mg g}^{-1}$ ),  $K_2$  is the Pseudo-second-order rate constant ( $\text{g mg}^{-1} \text{ min}^{-1}$ ). The initial adsorption rate,  $h$  ( $\text{mg g}^{-1} \text{ min}^{-1}$ ) at  $t \rightarrow 0$  is defined as:

$$h = K_2 q_e^2 \quad (2)$$

In the equation, the kinetic parameters  $h$ ,  $q_e$  and  $K_2$  can be obtained by linear plot of  $t/q_t$  versus  $t$ .

Fig. S2 is the plots of the Pseudo-second-order kinetics of CR adsorption by  $\text{Co}_x\text{Ni}_{1-x}$  alloy nanoparticles. The calculated kinetic parameters are listed in Table S2. The results present an ideal fit to the Pseudo-second-order kinetic for all adsorbents with  $r^2 > 0.97$ . A good agreement with this adsorption model is confirmed by the similar values of calculated  $q_e$  and the exper-

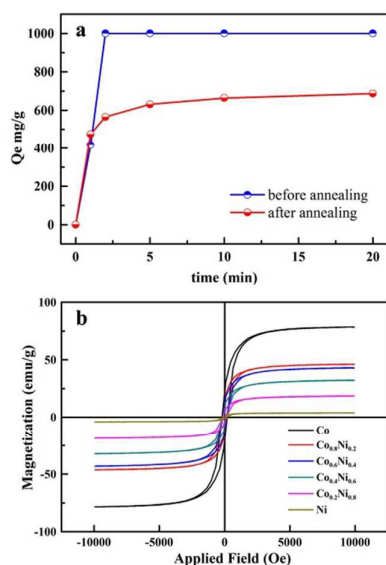


**Fig. 4** a) Adsorption ability for CR of the  $\text{Co}_{0.6}\text{Ni}_{0.4}$  nanoparticles before (blue line) and after (red line) annealing at 773 K for 2 h in argon atmosphere. (Initial dye concentration  $100 \text{ mg L}^{-1}$ , pH is about 7.5, temperature  $25 \text{ }^\circ\text{C}$ ) b) Hysteresis loops for the  $\text{Co}_x\text{Ni}_{1-x}$  nanoparticles measured at room temperature.

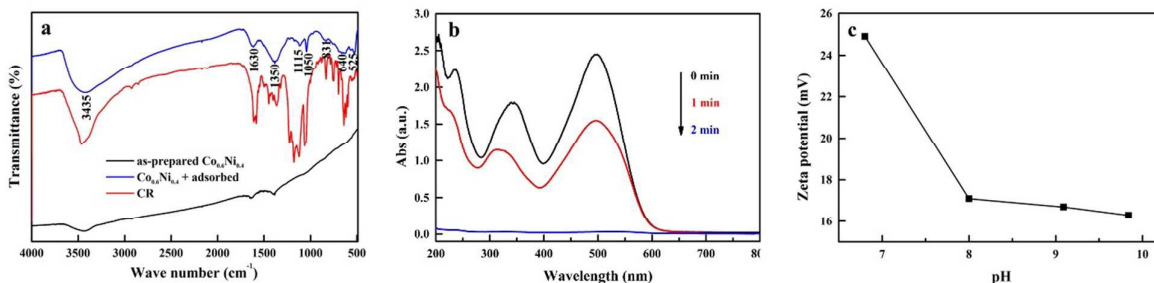
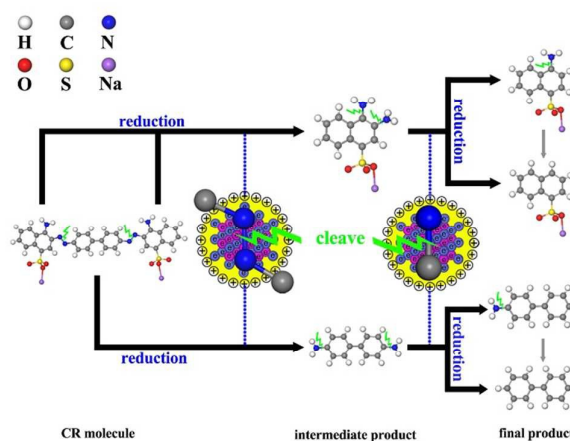


**Fig. 5** a) FT-IR spectra of Co<sub>0.6</sub>Ni<sub>0.4</sub> nanoparticles: before adsorption (black line) and after adsorption (blue line), and Congo Red (red line). b) Successive UV-vis spectra of CR removal in the presence of Co<sub>0.6</sub>Ni<sub>0.4</sub> after different time intervals, respectively. c) Zeta ( $\zeta$ )-potential of Co<sub>0.6</sub>Ni<sub>0.4</sub> nanoparticles as a function of solution pH. Total concentration of Co<sub>0.6</sub>Ni<sub>0.4</sub> nanoparticles is 100 mg L<sup>-1</sup>.

imental ones for adsorbent. The initial adsorption rate of all the samples is extremely high, while an increasing in the Ni content from 0 to 0.4, the initial adsorption rate increases from 601.14 to 1729.83 mg g<sup>-1</sup> min<sup>-1</sup>; further increase in the Ni content to 1 results in the decrease of initial adsorption rate to 497.26 mg g<sup>-1</sup> min<sup>-1</sup>. These consist with the ultrafast adsorption phenomenon. The best fit to the Pseudo-second-order kinetics indicates that the adsorption mechanism depends on the adsorbate and adsorbent.

**Adsorption mechanism.** To further shed light on the adsorption mechanism, FT-IR is carried out. Herein, FT-IR spectra of Co<sub>0.6</sub>Ni<sub>0.4</sub> nanoparticles before and after CR adsorption, as shown in Fig. 5a, are carefully investigated to expose the possible adsorption mechanism. For the as-prepared Co<sub>0.6</sub>Ni<sub>0.4</sub> nanoparticles (black line), the bond at 1630 cm<sup>-1</sup> is due to the O-H bend vibration of absorption water, and the bond at 1350 cm<sup>-1</sup> derives from the existence of the O-H bond of constituent water.<sup>44</sup> No metal oxide bonds exist in the FT-IR spectra. The as-synthesized nanoparticles are bimetallic alloys, which consists with the XRD results. When the nanoparticles were exposed to air, a thin oxidized layer was formed on the surface (XPS results), which made the nanoparticles air-stable. The CR-adsorbed Co<sub>0.6</sub>Ni<sub>0.4</sub> nanoparticles spectrum (blue line) and the CR spectrum (red line) are presented for comparison. The similar spectra demonstrate the well adsorption of CR by Co<sub>0.6</sub>Ni<sub>0.4</sub> nanoparticles. The presence of weak characteristic bonds at the range from 525 to 831 cm<sup>-1</sup> is believed to be associated with the stretching vibrations of Co<sup>2+</sup>-O<sup>2-</sup> and Ni<sup>2+</sup>-O<sup>2-</sup>. Hence, we may speculate that during the adsorption process oxidation and reduction reactions occur on the surface of Co<sub>0.6</sub>Ni<sub>0.4</sub> nanoparticles. Broad bond at 3435 cm<sup>-1</sup> can be attributed to the N-H stretching vibration while the bond at 1630 cm<sup>-1</sup> can be attributed to the C=C stretching vibration in benzene. The spectra at 1050 cm<sup>-1</sup> and 1115 cm<sup>-1</sup> are the featured peaks for CR, which reflects the SO<sub>3</sub><sup>-</sup> stretching modes in CR.<sup>45-47</sup> An evident difference is the decrease of the peaks located at 1050 cm<sup>-1</sup> and 1115 cm<sup>-1</sup>. These decreases may indicate the destruction of the CR structure by Co<sub>0.6</sub>Ni<sub>0.4</sub> nanoparticles. In order to clarify the changes of CR molecular structure during the adsorption process, the change in UV-vis spectra of solution

samples taken out at given time intervals was recorded (Fig. 5b). Three characteristic peaks of CR solution centered at 239, 340 and 497 nm are originated from aromatic rings, chromogenic group (-NH<sub>2</sub>) on aromatic rings and azo bonds (-N=N-), respectively.<sup>48</sup> Clearly, completely removal of CR occurred within 2 min by the as-prepared Co<sub>0.6</sub>Ni<sub>0.4</sub> nanoparticles. After 1 min of adsorption, all the adsorption peaks declined, and the peak located at 239 nm became the strongest, indicating that chromogenic group (-NH<sub>2</sub>) on aromatic rings and azo bands (-N=N-) were broken by the Co<sub>0.6</sub>Ni<sub>0.4</sub> nanoparticles during the process. And some aromatic rings had already been adsorbed on the surface of nanoparticles. Thereafter, the intensities of these bands decreased significantly and disappeared within 2 min. The electric potential near the surface (i.e.,  $\zeta$ -potential) of Co<sub>0.6</sub>Ni<sub>0.4</sub> nanoparticles as a function of solution pH is measured as an indicator of the surface potential and shown in Fig. 5c. The pH of CR solution used in the present experiment is measured to be about 7.5. As the surface of Co<sub>0.6</sub>Ni<sub>0.4</sub> nanoparticles is positively charged ( $\zeta$ -potential is about 20 mV) at the



**Scheme 2** Schematic adsorption mechanism on Co<sub>0.6</sub>Ni<sub>0.4</sub> nanoparticles (CR molecule and probable intermediate products are shown in Ball and Stick model).

current condition, a significantly strong electrostatic attraction appears between the adsorbent and the anionic CR molecule, which indicates the adsorption process begins with electrostatic attraction. The possible adsorption process and intermediate products are shown in Scheme 2. After CR was electrostatically absorbed on the surface of  $\text{Co}_{0.6}\text{Ni}_{0.4}$  nanoparticles, some  $\text{-N=N-}$  bonds were disconnected due to the high surface reactivity of  $\text{Co}_{0.6}\text{Ni}_{0.4}$  nanoparticles, resulting in the broken of the  $\pi$  bonds of characteristic conjugated chromophores in azo dye molecule. The particles would further destruct most of the chromogenic group ( $\text{-NH}_2$ ) on aromatic rings. Finally, the relative smaller dye groups, deriving from the decomposition of CR, adsorb on the particles chemically or electrostatically. Similar adsorption process for CR was reported in our previous study.<sup>49</sup> Hence, we speculate that reduction and electrostatic attraction happen at the same time, and chemical adsorption is the main adsorption mode for  $\text{Co}_{0.6}\text{Ni}_{0.4}$  nanoparticles during the CR removal process.

### 3.3 Calculations of surface properties

Although real adsorption mechanism depicts complex reactions, it is still useful to study the surface properties of the idealized model systems, if only for reference purposes. Here, we focus on investigating the difference of surface properties of model *fcc*-Co, *fcc*-Ni and *fcc*- $\text{Co}_{0.5}\text{Ni}_{0.5}$  with (111), (110) and (100) surfaces. Model *fcc*- $\text{Co}_{0.5}\text{Ni}_{0.5}$  is chosen to provide the information of the as-prepared  $\text{Co}_{0.6}\text{Ni}_{0.4}$  nanoparticles, which shows the best adsorption property in the present experiment. Since in the 28-atoms system the chemical composition of *fcc*- $\text{Co}_{0.5}\text{Ni}_{0.5}$  is closest to  $\text{Co}_{0.6}\text{Ni}_{0.4}$  nanoparticles, we believe it is feasible in theoretical explanation. To simulate the experimental poorly crystallized  $\text{Co}_{0.6}\text{Ni}_{0.4}$  nanoparticles, three kinds of previous theoretical calculations are larger than experimental

results, but in this work, our results give underestimate surface energies. Though the surface energy is sensitive to the calculation method, the obtained results are in completely quantitative agreement with experiment. It can be seen that the calculated (111) surface energy is the lowest in the three low index surfaces for all the three *fcc* structures. And this prediction is in accordance with the experiment consequence, (111) plane is the most stable surface of the three low index surfaces in *fcc* structure. Hence, in the following discussion we focus the investigation on (111) surface. Compared the three perfect (111) surface models, the surface energy follows the trend of *fcc*-Co > *fcc*- $\text{Co}_{0.5}\text{Ni}_{0.5}$  > *fcc*-Ni. Surprisingly, the surface energy of *fcc*- $\text{Co}_{0.5}\text{Ni}_{0.5}$  (1.91 J/m<sup>2</sup>) is closer to *fcc*-Ni of vacancy defects (namely  $V_{\text{Co}}$ ,  $V_{\text{Ni}}$  and  $V_{\text{CoNi}}$ ) are introduced into (111) surface of model *fcc*- $\text{Co}_{0.5}\text{Ni}_{0.5}$ , which is used for revealing the relationships between defects and surface properties (such as surface energy, work function and electronic structure).

**Surface energy.** We determine the stability of a surface by calculated the surface energy, defined as:

$$\gamma = \frac{E_{\text{surf}} - 0.5 \sum n_M E_M^{\text{bulk}} - 0.5 E_{\text{surf}}^{\text{unrel}}}{A} \quad (3)$$

where  $E_{\text{surf}}$  is the total energy of relaxed surface slab,  $E_M^{\text{bulk}}$  is the energy of reference atom in bulk,  $n_M$  is the number of atoms contained in the surface model ( $M$  represents Co or Ni).  $E_{\text{surf}}^{\text{unrel}}$  is the total energy of the un-relaxed surface slab and  $A$  is the surface area. The factor 0.5 accounts for the fact that only the upper part of the model is allowed to relax while the rest is fixed to the bulk positions. For comparison, our calculated surface energies of all surface models as well as some previous theoretical and experimental results are summarized in Table 1. From this table, one can notice that the surface energies of *fcc*-Co and *fcc*-Ni given

**Table 1** Surface energies and work functions for the calculated surfaces, this work, previous theory calculation and experimental.

Models	Surface	Surface energy (J/m <sup>2</sup> )			Work function (eV)		
		This work	Theory <sup>a</sup>	Expt. <sup>b</sup>	This work	Theory <sup>a</sup>	Expt. <sup>b</sup>
<i>fcc</i> -Co	(111)	2.05	2.70		5.10	5.55	
	(110)	2.37		2.55 ( <i>hcp</i> )	4.46		5.0 ( <i>hcp</i> )
	(100)	2.46	2.78		4.27	5.52	
<i>fcc</i> -Ni	(111)	1.88	2.69	2.45	5.12	5.70	5.35
	(110)	2.24			4.56		
	(100)	2.18	2.77		4.98	5.75	
<i>fcc</i> - $\text{Co}_{0.5}\text{Ni}_{0.5}$	(111)	1.90			5.08		
	(110)	2.26			4.48		
	(100)	2.24			4.69		
$V_{\text{Co}}$	(111)	2.29			4.82		
$V_{\text{Ni}}$	(111)	2.37			4.87		
$V_{\text{CoNi}}$	(111)	2.44			4.56		

<sup>a</sup> See Ref 50.

<sup>b</sup> See Ref 26.

(1.88 J/m<sup>2</sup>), which may explain why the *fcc*-Ni is more stable than the naturally unstable *fcc*-Co (metallic Co is more stable in *hcp* phase). The atom radius of Co (1.25 Å) and Ni (1.24 Å) are close to each other, then the *fcc*-Co<sub>0.5</sub>Ni<sub>0.5</sub> alloy originating from the replacement of Co at Ni position does not change the *fcc*-Ni structure a lot, which is consistent with our experimental result, resulting in a similar (111) surface energy. When vacancies are introduced into the perfect surface, the surface energies become higher. The more vacancies in the surface, the higher the surface energy got. This theory suggests that the Co<sub>0.6</sub>Ni<sub>0.4</sub> alloy nanoparticles contain many vacancy defects in their surfaces equipped with an exceptional high surface energy.

**Work function.** The work function of the surface models are also calculated and listed in Table 1. The work function,  $\Phi$ , describes the ability or tendency of an electron to escape from a material, and reflects the stability of the surface electrons.<sup>51</sup> The higher the value of work function is, the more stable the surface electrons are. The formula for the work function is as follows:

$$\Phi = E_{vac}(+\infty) - E_F \quad (4)$$

where  $E_{vac}$  is the vacuum energy, it was calculated as the averaged electrostatic potential in the middle of the vacuum region, and  $E_F$  is the corresponding Fermi energy. The calculated work function for the surface is listed in Table 1. The results obtained in current calculation, quantitatively, are in very good agreement with previous experimental and theoretical values. Since the work function of (111) surface is higher than the other two surfaces, the surface electrons are more stable, further implying that (111) is the most stable surface of the three low index surfaces in *fcc* structure. Compared the three

perfect (111) surface models, the work function exhibits the order *fcc*-Ni > *fcc*-Co > *fcc*-Co<sub>0.5</sub>Ni<sub>0.5</sub>, which means that the coexistence of Co and Ni in the (111) surface makes the surface electrons unstable, then we may speculate that Co<sub>0.6</sub>Ni<sub>0.4</sub> alloy has better activity than those of pure Ni and Co. Further calculations show that vacancy defects in the surface make the work function sharply decreased, implying vacancy defects would make the surface more instable, which consist with the surface energy results. Generally, increase of surface energy and decrease of work function would lead the surface more active. As previous report demonstrates that the smaller work function makes the metal a stronger chemical reducing agent and a poorer oxidizing agent.<sup>23</sup> Hence, we conclude that the Co<sub>0.6</sub>Ni<sub>0.4</sub> alloy nanoparticles synthesized at room temperature are equipped with high surface energy and small work function, and during the adsorption process the nanoparticles play as strong chemical reducing agents.

**Densities of states.** Fig. 6a to 6c show the total densities of states (TDOS) and partial densities of states (PDOS) for bulk Co, Ni and Co<sub>0.5</sub>Ni<sub>0.5</sub>, respectively. It's clearly seen that all the TDOS curves for spin-up and spin-down are unsymmetric. The spin-polarization around the Fermi level implies the existence of magnetism and the lack of a band gap near the Fermi level signals that the bulk cells have a metallic characteristic. Compared with PDOS curves, the valence band is mainly composed of Co or Ni 3*d*-orbital electrons. Since the valence electronic configurations for Co and Ni are 3*d*<sup>7</sup>4*s*<sup>2</sup> and 3*d*<sup>8</sup>4*s*<sup>2</sup>, the 3*d*-orbital is partially occupied and above Fermi level is empty. The 3*d*-orbital of bulk Co<sub>0.5</sub>Ni<sub>0.5</sub> is slightly changed comparing with the bulk Co and Ni, and the main variation occurs at the spin-down orbital. Fig. 6d shows the detail composition of the

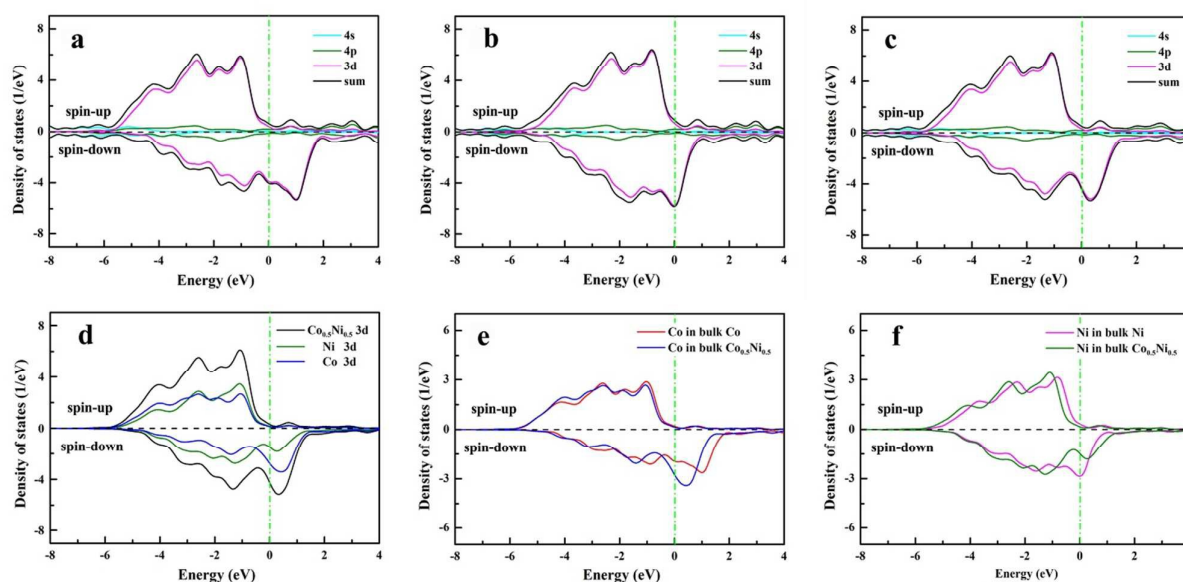


**Fig. 6** TDOS and PDOS of a) bulk Co, b) bulk Ni and c) bulk Co<sub>0.5</sub>Ni<sub>0.5</sub>. 3*d*-orbital PDOS of d) Co and Ni in bulk Co<sub>0.5</sub>Ni<sub>0.5</sub>, e) Co in bulk Co and Co<sub>0.5</sub>Ni<sub>0.5</sub> and f) Ni in bulk Ni and Co<sub>0.5</sub>Ni<sub>0.5</sub>. For clarity, the intensity of bulk Co and Ni in e and f are reduced to half for comparison. The vertical dash-dot green line at E=0 eV, represent Fermi level.

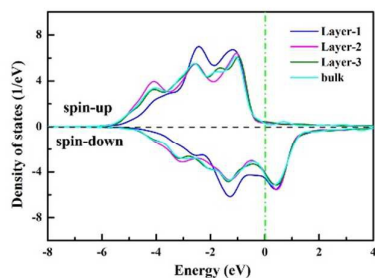


Fig. 7 3d-orbital PDOS of Layer-1, Layer-2, Layer-3 and bulk Layer of  $\text{Co}_{0.5}\text{Ni}_{0.5}$  (111) surface. The vertical dash-dot green line at  $E=0$  eV, represent Fermi level.

bulk  $\text{Co}_{0.5}\text{Ni}_{0.5}$  3d-orbital of Co and Ni. Obviously, Co 3d-orbital overlaps with Ni 3d-orbital, implying the interaction between Co and Ni is strong. Fig. 6e and 6f present the 3d-orbital difference of Co and Ni between pure metal and  $\text{Co}_{0.5}\text{Ni}_{0.5}$ , respectively. The main changes locate near the Fermi level, compared with pure metal, the density state of Ni in  $\text{Co}_{0.5}\text{Ni}_{0.5}$  around Fermi level is weakened, on the contrary, the density state of Co is enhanced. The change may originate from the difference of electronegativity between Ni (1.91) and Co (1.88). As a result, the electronics and holes which participated in the reaction around the Fermi level increased, thus the activity of  $\text{Co}_{0.5}\text{Ni}_{0.5}$  rises.

To have a better insight into the  $\text{Co}_{0.5}\text{Ni}_{0.5}$  (111) surface, PDOS of the 3d-orbital of the outer three layers are compared with the deep bulk layer, the calculated results are plotted in Fig. 7. Compared with the PDOS curves of the bulk layer, Layer-2 and Layer-3 are similar to the deep bulk layer, but the curve of outermost layer (Layer-1) has an apparent difference. For Layer-1, the density of states located at the high energy region ( $-3 \sim 0$  eV) is obviously enhanced, however, in the low energy region ( $< -3$  eV) the intensity of the electronic density is weakened. The changes of the density of states in high energy and low energy regions make the surface structure exhibit an unstable and high energy state, and Layer-1 is dominant in the surface property. In addition, the  $\text{Co}_{0.5}\text{Ni}_{0.5}$  (111) surface with Ni and Co vacancy defects ( $V_{\text{CoNi}}$ ) in Layer-1 is also calculated, and the 3d-orbital PDOS of Layer-1 is shown below. The density of states is mainly concentrated in the high energy region ( $-3 \sim 0$  eV). As for the surfaces, the difference of the PDOS above the Fermi level is not quite distinct.

**Electron density difference.** To obtain a qualitative perspective on the extent of charge transfer of the surfaces, electron density difference is calculated and plotted in Fig. 8. The density contours for the three perfect (111) surfaces (Fig. 8a) clearly show the electrons accumulation into the interstitial regions, indicating the metallic bonding. For  $\text{Co}_{0.5}\text{Ni}_{0.5}$  (111) surface, due to the difference of the electronegativity, redistribution of charge happens in the Co and Ni cores. Compared with the pure Co and Ni, it can be concluded that parts of electrons transfer from Co atom to Ni atom, but along the Co-Co bond electrons accumulate localized in Co cores while along Co-Ni

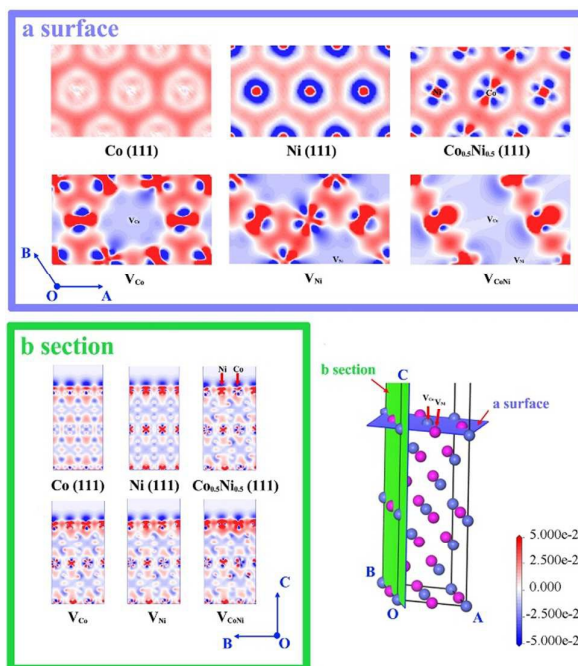
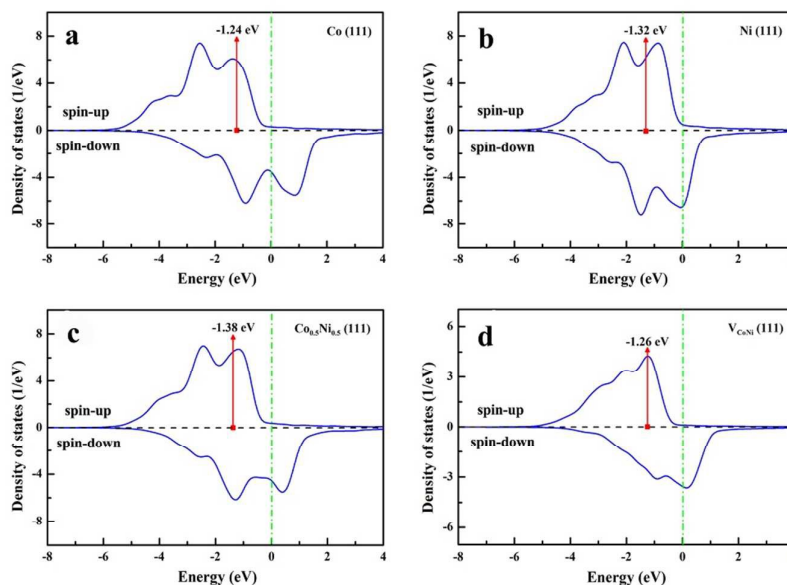


Fig. 8 The plot of electron density difference. a) (111) surface. b) section. The loss and enrichment of electrons are indicated in blue and red.

bond electrons of Co cores deplete. The results consist with the above PDOS analysis of bulk  $\text{Co}_{0.5}\text{Ni}_{0.5}$ . When vacancy defects occur in  $\text{Co}_{0.5}\text{Ni}_{0.5}$  (111) surface, the electrons become more localized accumulation in Ni cores, and the accumulation of electrons in the interstitial regions between atoms indicates the existence of metallic bonding. Fig. 8b presents the section electron density difference of both perfect and defect surfaces. Obviously, charge accumulates on surface atom cores, resulting in high surface activity, which is in agreement with the surface energy and work function conclusion. It can be noted that in  $\text{Co}_{0.5}\text{Ni}_{0.5}$  (111) surface the electrons accumulate in Ni cores more than that in Co cores. But when the introduction of vacancy defects, the electrons accumulate in the surface Co atoms also enhanced along Co-Ni bond, while vertical to the (111) surface more electrons depleted. More electrons accumulate in the cores of surface atoms, which indicate that the existence of Ni and defects in the surface make the surface more active. In other words, the  $\text{Co}_{0.6}\text{Ni}_{0.4}$  bimetallic alloys with poor crystallization own higher reducibility than mono-metal Co and Ni.

**d-band centers.** The d-band centers of the surfaces are also calculated, as shown in Fig. 9. The calculated d-band center of Co and Ni (111) surface (see Fig. 9a and 9b) is  $-1.24$  and  $-1.32$  eV, respectively. These values are in good agreement with the previous theoretical results ( $-1.17$  eV for Co and  $-1.29$  eV for Ni).<sup>52</sup> The calculated d-band center for  $\text{Co}_{0.5}\text{Ni}_{0.5}$  (111) surface is  $-1.38$  eV, that is, the formation of  $\text{Co}_{0.5}\text{Ni}_{0.5}$  alloy moves the d-band center away from Fermi level. As the introduction of



**Fig. 9** 3d-orbital PDOS of the outermost layer (Layer-1) of a) Co (111) surface, b) Ni (111) surface, c)  $\text{Co}_{0.5}\text{Ni}_{0.5}$  (111) surface and d)  $\text{Co}_{0.5}\text{Ni}_{0.5}\text{-VCoNi}$  (111) surface. The red line marks  $d$ -band center. The vertical dash-dot green line at  $E=0$  eV, represent Fermi level.

vacancies into the  $\text{Co}_{0.5}\text{Ni}_{0.5}$  (111) surface, the  $d$ -band center changes from  $-1.38$  to  $-1.26$  eV. The width and center of  $d$ -band are highly correlated to each other due the fact that the  $d$ -band filling changes negligibly upon the formation of these bimetallic surfaces.<sup>53</sup> As seen in Fig. 9, when bimetallic surface is formed, the combined effects result in a broader  $d$ -band, so the  $d$ -band center moves to low energy. In contrast,  $d$ -band is narrowed due to the defects and shifts to high energy. It is known that the  $d$ -band center is a measure of the reactivity for the transition metals. Surface atoms with larger coordination number have lower  $d$ -band center and weaker adsorption ability.<sup>52</sup> The existence of vacancies in the surface leads  $d$ -band center closer to Fermi level, meanwhile enhances the adsorption ability of the surface.

### 3.4 Summary

According to the above experimental and theoretical results, the enhanced ability may be explained as follows. The adsorption process begins with strong electrostatic attraction of anionic CR molecules, since the surface of  $\text{Co}_{0.6}\text{Ni}_{0.4}$  nanoparticles is positively charged ( $\zeta$ -potential is about 20 mV). In the bimetallic alloy nanoparticles, Co and Ni atoms strongly interact with each other, and the low degree of crystallinity leads plenty of vacancies in the surface, making them with large surface energy and low work function. As it is known, the large surface energy makes the particle unstable, then the surface tends to adsorb (physically and chemically) adsorbate to decrease the surface energy forming an equilibrium state. And as the surface is abundance of vacancies, the work function is relatively low, indicating the instable of the surface electrons. By the calculation of DOS, PDOS and electron density difference, clearly the co-existence of Co and Ni leads strong

interaction and charge separation between them, electrons tend to transfer from Co to Ni. And in the surface electrons accumulate in the surface atom cores, making the nanoparticles a strong reducing agent with relative high activity. And with the relatively high specific areas ( $60.6 \text{ m}^2 \text{ g}^{-1}$ ), the activity sites participating in the adsorption process are increased. It is also known that the  $d$ -band center is the key parameter that determines the kinetics of the oxygen-reduction reaction.<sup>54</sup> Experiment for the adsorption of CR with bimetallic nanoparticles includes chemisorption and electrostatic attraction at the same time. Here the chemisorption is denoted as reduction process. When the  $d$ -band center is too close to the Fermi level, the binding between the surface and adsorbate is too strong, so the reaction rate is limited by the removing rate of surface intermediate. On the contrary, when the  $d$ -band center is too far to the Fermi level, the binding between the surface and adsorbate is too weak, thereby the reaction rate is limited by the rate of electrons transfer to adsorbate. The presence of vacancies causes the shift of  $d$ -band center close to the Fermi level, which can enhance both the chemisorption and electrostatic attraction. In the present CR removal process as mentioned above (Scheme 2), chemisorption and electrostatic attraction occur at the same time, and chemisorption is the main adsorption mode. In a word, the as-synthesized  $\text{Co}_{0.6}\text{Ni}_{0.4}$  bimetallic alloy nanoparticles show high adsorption efficiency due to its positively charged surface, large surface energy, low work function, high reducibility, high specific areas and a modified  $d$ -band center satisfied both the highly efficient electrons transfer of nanoparticles to CR and quick removal of surface intermediate.

## 4. Conclusions

Co<sub>x</sub>Ni<sub>1-x</sub> alloy nanoparticles with a poorly crystallized nature are prepared by a NaBH<sub>4</sub> reduction method at room temperature. Significantly, the bimetallic alloys can completely adsorb 100 mL g<sup>-1</sup> of CR aqueous solution within 2 to 20 min, and 1000 mg g<sup>-1</sup> of adsorption capacities can be achieved. After the adsorption, Co<sub>x</sub>Ni<sub>1-x</sub> alloy nanoparticles with CR also can be magnetically separated from aqueous solution. With the aid of DFT simulations, we may find that the chemical composition and vacancy defects have important influences on the surface properties (such as surface energy, work function and electronic structure), and it can be concluded that the experimental Co<sub>0.6</sub>Ni<sub>0.4</sub> bimetallic alloy nanoparticles with chemical composition similar to the model *fcc*-Co<sub>0.5</sub>Ni<sub>0.5</sub> have larger surface energy, lower work function and higher reducibility than monometal Co and Ni. Furthermore, the high adsorption capability and efficiency of Co<sub>0.6</sub>Ni<sub>0.4</sub> alloy nanoparticles are because that the modified *d*-band center maybe satisfied both the highly efficient electrons transfer of alloy nanoparticles to CR and quick removal of surface intermediate. These low-cost adsorbents with high efficient and ultrafast adsorption show a bright future of commercial scale waste water treatment.

### Acknowledgements

This work was financially supported by National Natural Science Foundation of China (Grant No.51501068) and the Foundation of National Key Basic Research and Development Program (Grant No.2010CB631001).

### References

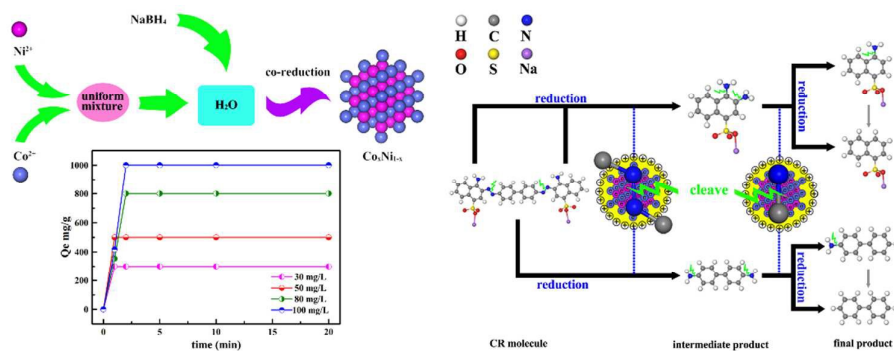
- C. X. Peng, B. D. Chen, Y. Qin, S. H. Yang, C. Z. Li, Y. H. Zuo, S. Y. Liu and J. H. Yang, *ACS Nano*, 2012, **6**, 1074-1081.
- Y. Y. Liang, Y. G. Li, H. L. Wang, J. G. Zhou, J. Wang, T. Regier and H. J. Dai, *Nature Mater.*, 2011, **10**, 780-786.
- N. Li, C. W. Hu and M. H. Cao, *Phys. Chem. Chem. Phys.*, 2013, **15**, 7685-7689.
- M. Raula, M. H. Rashid, S. Lai, M. Roy and T. K. Mandal, *ACS Appl. Mater. Interfaces*, 2012, **4**, 878-889.
- S. K. Singh, A. K. Singh, K. Aranishi and Q. Xu, *J. Am. Chem. Soc.*, 2011, **133**, 19638-19641.
- H. Li, J. Liao, Y. Du, T. You, W. Liao and L. Wen, *Chem. Commun.*, 2013, **49**, 1768-1770.
- F. Bao, J.-F. Li, B. Ren, Jian-Lin Yao, R.-A. Gu and Z.-Q. Tian, *J. Phys. Chem. C*, 2008, **112**, 345-350.
- N. Toshima and T. Yonezawa, *New J. Chem.*, 1998, **22**, 1179-1201.
- N. J. Costa, M. Guerrero, V. Collière, É. Teixeira-Neto, R. Landers, K. Philippot and L. M. Rossi, *ACS Catal.*, 2014, **4**, 1735-1742.
- V. Mazumder, M. Chi, K. L. More and S. Sun, *J. Am. Chem. Soc.*, 2010, **132**, 7848-7849.
- R. W. Scott, C. Sivadinarayana, O. M. Wilson, Z. Yan, D. W. Goodman and R. M. Crooks, *J. Am. Chem. Soc.*, 2005, **127**, 1380-1381.
- J. Zhang, H. Yang, J. Fang and S. Zou, *Nano Lett.*, 2010, **10**, 638-644.
- R. Ferrando, J. Jellinek and R. L. Johnston, *Chem. Rev.*, 2008, **108**, 845-910.
- H. Q. Yu and H. H. Fang, *Appl. Microbiol. Biot.*, 2000, **54**, 439-444.
- G. H. Chen, *Sep. Purif. Technol.*, 2004, **38**, 11-41.
- M. Arami, N. Y. Limaee, N. M. Mahmoodi and N. S. Tabrizi, *J. Colloid Interface Sci.*, 2005, **288**, 371-376.
- Z. H. Hu, H. Chen, F. Ji and S. J. Yuan, *J. Hazard. Mater.*, 2010, **173**, 292-297.
- J. M. Gomez, J. Galan, A. Rodriguez and G. M. Walker, *J. Environ. Manage.*, 2014, **146**, 355-361.
- C. Wang, Y. Le and B. Cheng, *Ceram. Int.*, 2014, **40**, 10847-10856.
- J. X. Shu, Z. H. Wang, Y. J. Huang, N. Huang, C. G. Ren and W. Zhang, *J. Alloy. Compd.*, 2015, **633**, 338-346.
- X. M. Liang and L. J. Zhao, *Rsc Advances*, 2012, **2**, 5485-5487.
- A. H. M. A. Wasey, S. Chakrabarty, G. P. Das and C. Majumder, *ACS Appl. Mater. Interfaces*, 2013, **5**, 10404-10408.
- Y. Yoon, R. Rousseau, R. S. Weber, D. H. Mei and J. A. Lercher, *J. Am. Chem. Soc.*, 2014, **136**, 10287-10298.
- J. M. Hernandez, D. H. Lim, H. V. P. Nguyen, S. P. Yoon, J. Han, S. W. Nam, C. W. Yoon, S. K. Kim and H. C. Ham, *Int. J. Hydrogen Energy*, 2014, **39**, 12251-12258.
- V. A. Ranea, *J. Mol. Catal. A-chem.*, 2014, **392**, 157-163.
- H. Skriver and N. Rosengaard, *Phys. Rev. B*, 1992, **46**, 7157-7168.
- I. E. L. Stephens, A. S. Bondarenko, U. Gronbjerg, J. Rossmeisl and I. Chorkendorff, *Energ. Environ. Sci.*, 2012, **5**, 6744-6762.
- S. J. Yoo, S. K. Kim, T. Y. Jeon, S. J. Hwang, J. G. Lee, S. C. Lee, K. S. Lee, Y. H. Cho, Y. E. Sung and T. H. Lim, *Chem. Commun.*, 2011, **47**, 11414-11416.
- B. B. Xiao, Y. F. Zhu, X. Y. Lang, Z. Wen and Q. Jiang, *Sci. Rep.*, 2014, **4**, 5205.
- N. Troullier and J. L. Martins, *Phys. Rev. B*, 1991, **43**, 1993-2006.
- M. D. Segall, P. J. D. Lindan, M. J. Probert, C. J. Pickard, P. J. Hasnip, S. J. Clark and M. C. Payne, *J. Phys-condens. Mater.*, 2002, **14**, 2717-2744.
- S. J. Clark, M. D. Segall, C. J. Pickard, P. J. Hasnip, M. J. Probert, K. Refson and M. C. Payne, *Z. Kristallogr.*, 2005, **220**, 567-570.
- J. P. Perdew and Y. Wang, *Phys. Rev. B*, 1992, **45**, 13244-13249.
- J. P. Perdew, K. A. Jackson, M. R. Pederson, D. J. Singh and C. Fiolhais, *Phys. Rev. B*, 1992, **46**, 6671-6687.
- D. Kim, S. L. Shang and Z. K. Liu, *Comp. Mater. Sci.*, 2009, **47**, 254-260.
- W. X. Zhang, Z. H. Jiang, G. Y. Li, Q. Jiang and J. S. Lian, *Appl. Surf. Sci.*, 2008, **254**, 4949-4955.
- S. Rives, A. Catherinot, F. Dumas-Bouchiat, C. Champeaux, A. Videcoq and R. Ferrando, *Phys. Rev. B*, 2008, **77**, 085407.
- J. M. Yan, X. B. Zhang, S. Han, H. Shioyama and Q. Xu, *J. Power Sources*, 2009, **194**, 478-481.
- J. Du, F. Y. Cheng, M. Si, J. Liang, Z. L. Tao and J. Chen, *Int. J. Hydrogen Energy*, 2013, **38**, 5768-5774.
- T. Chuang, C. Brundle and D. Rice, *Surf. Sci.*, 1976, **59**, 413-429.
- G. Ertl, R. Hierl, H. Knözinger, N. Thiele and H. Urbach, *Applications of Surface Science*, 1980, **5**, 49-64.
- L. Y. Qin, J. S. Lian, Z. H. Jiang, G. Y. Wang and Q. Jiang, *J. Mater. Res.*, 2010, **25**, 401-405.
- Y.-S. Ho and G. McKay, *Process Biochem.*, 1999, **34**, 451-465.
- B. C. Smith, *Infrared Spectral Interpretation: A Systematic Approach*, CRC Press, Boca Raton, 1999.
- F. H. Li, Y. Bao, J. Chai, Q. X. Zhang, D. X. Han and L. Niu, *Langmuir*, 2010, **26**, 12314-12320.
- S. D. Deng, X. H. Li and H. Fu, *Corros. Sci.*, 2011, **53**, 760-768.
- J. Sajid, A. Elhaddaoui and S. Turrell, *J. Mol. Struct.*, 1997, **408-409**, 181-184.
- Z. J. Li, X. W. Zhang, J. Lin, S. Han and L. C. Lei, *Bioresource Technol.*, 2010, **101**, 4440-4445.

## ARTICLE

Journal Name

- 49 L. X. Wang, J. C. Li, C. S. Mao, L. S. Zhang, L. J. Zhao and Q. Jiang, *Dalton. Trans.*, 2013, **42**, 8070-8077.
- 50 M. Alde'n, S. Mirbt, H. Skriver, N. Rosengaard and B. Johanson, *Phys. Rev. B*, 1992, **46**, 6303-6312.
- 51 J. L. F. Da Silva, *Phys. Rev. B*, 2005, **71**, 195416.
- 52 B. Hammer and J. K. Norskov, *Adv. Catal.*, 2000, **45**, 71-129.
- 53 J. R. Kitchin, J. K. Norskov, M. A. Barteau and J. G. Chen, *Phys. Rev. Lett.*, 2004, **93**, 156801.
- 54 V. R. Stamenkovic, B. S. Mun, M. Arenz, K. J. J. Mayrhofer, C. A. Lucas, G. F. Wang, P. N. Ross and N. M. Markovic, *Nature Mater.*, 2007, **6**, 241-247.

## Table of Contents Graphic and Synopsis



The high efficient and ultrafast adsorption performance of the synthesized bimetallic alloys: An experimental and theoretical study.